

## WALL-HEATED/COOLED EFFECTS ON LOW-FREQUENCY PRESSURE FLUCTUATIONS IN SHOCK-WAVE AND TURBULENT BOUNDARY LAYER INTERACTIONS

**Ryo Hirai**

Department of Aerospace Engineering  
Tohoku University  
Sendai Miyagi 980-8579, Japan  
ryo.hirai.q7@dc.tohoku.ac.jp

**Soshi Kawai**

Department of Aerospace Engineering  
Tohoku University  
Sendai Miyagi 980-8579, Japan  
kawai@tohoku.ac.jp

### ABSTRACT

Direct numerical simulations of shock-wave and turbulent boundary layer interactions with wall heat flux are performed to investigate wall heat flux effects on low-frequency dynamics of shock interacted flows. We compare three wall temperature cases of quasi-adiabatic, heated, and cooled conditions under the freestream Mach number  $M_\infty = 2.28$  and Reynolds number  $Re_\theta \approx 5,000$ . The results focusing on low-frequency dynamics of flow and pressure fields suggest that boundary layer separations and reflected shock are associated with low-frequency wall pressure fluctuations. Also, high-frequency wall pressure fluctuations originate from turbulent structures at separated shear layers and attached boundary layers. The results and discussion suggest that wall temperature effects on pressure gradients of reflected shock and the semi-local Reynolds number can change the low- and high-frequency wall pressure fluctuations, respectively.

### INTRODUCTION

In many aerospace applications, shock-wave and turbulent boundary layer interactions (SWBLIs) significantly affect the aerodynamic and thermodynamic performance by inducing flow separations that increase drag and heat exchanges at wall surfaces. Also, the unsteady flow fields provide pressure fluctuations, including low-frequency components at least two-order lower than dominant frequencies of attached turbulent boundary layers. The low-frequency pressure fluctuations can lead to structural fatigue when coupling to resonant frequencies of aircraft wings or overexpanded rocket nozzles (Deck, 2009). Thus, detailed mechanisms of low-frequency unsteadiness in SWBLIs should be elucidated to reduce undesirable structural oscillations.

Flow physics of SWBLIs has been investigated by experimental and numerical studies over the last few decades. Recently, driving mechanisms of the low-frequency unsteadiness have been proposed in two categories: a forcing mechanism from upstream or downstream (Clemens and Narayanaswamy,

2014). Regarding the upstream forcing mechanism, some previous studies have shown correlations between upstream flow properties and the shock-foot motion (Brusniak and Dolling, 2006; Toubert and Sandham, 2011). Also, the existence of long coherent flow structures, whose length is approximately 40 times as long as boundary layer thickness, is observed experimentally at attached boundary layer flows (Ganapathisubramani *et al.*, 2007 & 2009). The authors reported that the large structures flow into the shock interacted regions and influence the upstream or downstream shifts of the separation point. In contrast, some downstream forcing mechanisms focus on boundary layer separations that lift wall turbulence to outer boundary layers and generate separation bubbles. For example, a low-frequency oscillation model has been proposed based on the properties of fluid entrainment in shock-induced separation bubbles (Piponnier *et al.*, 2009). Another work proposed an acoustic feedback mechanism associated with incident shock oscillations by passages of uplifted vortex structures (Pirozzoli & Grasso, 2006).

As shown above, the low-frequency unsteadiness of SWBLIs has been actively researched in the last two decades. However, most of the studies address cases of adiabatic wall conditions. In a practical situation of rocket nozzles, a wall cooling system is often equipped to decrease the damage caused by thermal loads. The wall heat flux can affect shock-interacted boundary layer flows at an inner wall of the nozzle and changes the characteristics of low-frequency pressure fluctuations, thus, we need to understand the detailed contributions of wall heat flux to the flow physics of SWBLIs. In a previous study of SWBLIs with wall-thermal conditions, wall heating and cooling effects on the shock-induced flow separations are reported; the separated regions get larger and smaller in heated and cooled wall cases, respectively (Bernardini *et al.*, 2016). Also, Jaunet and Volpiani *et al.* reported influences of wall heat flux on wall pressure fluctuations whose spectral distributions shift to lower and higher frequencies in the heated and cooled case, respectively, compared with the adiabatic case (Jaunet *et al.*, 2014; Volpiani *et al.*, 2018). However, detailed

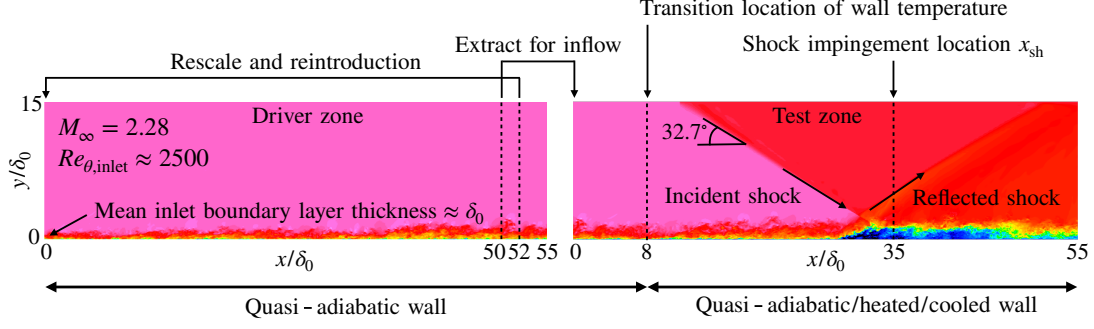


Figure 1. Computational domain of present DNS. Mean streamwise velocity contours.

mechanisms of wall heat flux to affect flow physics driving the low-frequency unsteadiness of SWBLIs have not been elucidated. Therefore, We should investigate how wall heating or cooling affects the SWBLIs to evaluate wall heat flux contributions to controlling low-frequency oscillations induced by shock interactions.

In this study, direct numerical simulation (DNS) of oblique shock-wave and turbulent boundary layer interactions on a heated or cooled flat wall is conducted to investigate wall heat flux effects on low-frequency dynamics of shock-wave interacted turbulent boundary layer flows. We perform three different wall temperature cases (i.e., quasi-adiabatic, heated, and cooled) under the freestream Mach number  $M_\infty = 2.28$  and Reynolds number  $Re_\theta \approx 5,000$  conditions and evaluate differences in mean flow fields and low-frequency fluctuation properties by comparing the cases.

## COMPUTATIONAL STRATEGY

### Governing equations

In the present study, we carry out direct numerical simulations by solving the following compressible Navier-Stokes equations as

$$\frac{\partial \rho}{\partial t} + \frac{\partial (\rho u_j)}{\partial x_j} = 0, \quad (1)$$

$$\frac{\partial (\rho u_i)}{\partial t} + \frac{\partial (\rho u_i u_j + p \delta_{ij} - \tau_{ij})}{\partial x_j} = 0, \quad (2)$$

$$\frac{\partial (\rho E)}{\partial t} + \frac{\partial (\rho E u_j + p u_j + q_j - u_i \tau_{ij})}{\partial x_j} = 0, \quad (3)$$

where  $\rho$  is the density,  $p$  is the pressure, and  $E$  is the total energy. The streamwise, wall-normal, and spanwise coordinates are denoted by  $x_j = (x, y, z)$  respectively, and  $u_i = (u, v, w)$  are the corresponding velocity components. The pressure  $p$  is given by the equation of state of ideal gas as

$$p = \rho R T, \quad (4)$$

where  $R$  is the gas constant and  $T$  is the temperature. The viscous stress tensor  $\tau_{ij}$  and heat flux vector  $q_j$  are given as

$$\tau_{ij} = 2\mu \left[ \frac{1}{2} \left( \frac{\partial u_i}{\partial x_j} + \frac{\partial u_j}{\partial x_i} \right) - \frac{1}{3} \frac{\partial u_k}{\partial x_k} \delta_{ij} \right], \quad (5)$$

$$q_j = -\frac{\mu}{Pr(\gamma-1)} \frac{\partial a^2}{\partial x_j}, \quad (6)$$

where  $\mu$  is the dynamic viscosity,  $a$  is the speed of sound, and  $Pr (= 0.72)$  is the Prandtl number. The dynamic viscosity is given by Sutherland's law as

$$\frac{\mu}{\mu_\infty} = \left( \frac{T}{T_\infty} \right)^{\frac{3}{2}} \frac{T_\infty + T_1}{T + T_1}, \quad (7)$$

where  $T_\infty = 255.0 [K]$  and  $T_1 = 110.4 [K]$ . The subscript  $\infty$  denotes the freestream quantities.

### Case settings

Figure 1 shows the schematic of the present simulations of oblique shock-wave and turbulent boundary layer interaction on a flat plate with wall heat flux. There are two divided zones (i.e., driver and test zones) whose domain size is  $(L_x, L_y, L_z) = (55\delta_0, 15\delta_0, 6\delta_0)$ , where  $\delta_0$  is approximately equal to the inlet boundary layer thickness of driver zone. In driver zone (on left in Fig. 1), the incoming turbulent boundary layers are generated by the rescaling-reintroduction method (Urbin & Knight, 2001) under quasi-adiabatic wall conditions. The rescale length  $x = 52\delta_0$  is decided to eliminate the artificial streamwise contamination caused by the reintroduction (Simens *et al.*, 2009). The turbulent boundary layer flows at  $x = 50\delta_0$  downstream of driver zone are given directly to the inlet of test zone (on right in Fig. 1). In test zone, the wall temperature is transitioned from the quasi-adiabatic condition to the heated and cooled conditions at  $x = 8\delta_0$  downstream. The quasi-adiabatic, heated, and cooled wall temperatures are defined based on the recovery temperature as

$$T_r = T_\infty \left[ 1 + (\gamma-1)r \frac{M_\infty^2}{2} \right], \quad (8)$$

where  $r (= 0.9)$  is the recovery coefficient. Also, incident shock-wave generated at the upper boundary impinges on the lower wall at  $x_{sh} = 35\delta_0$  downstream with  $32.7^\circ$  angles when assuming the inviscid wall conditions. In both zones, periodic and outflow conditions are imposed in the spanwise and outlet boundaries, respectively.

The sixth-order compact scheme is used for spatial discretization with the eighth-order compact low-pass filter, where a filter coefficient is set to 0.495 (Lele, 1992; Gaitonde & Visbal, 1999; Kawai & Fujii, 2008). The localized artificial diffusivity method is employed to capture shock waves

Table 1. Flow and grid parameters for present DNS.  $L_{\text{int}}$ , the interaction length;  $N$ , number of grid points in test zone; subscript  $w$ , properties taken at wall.

Case	$M_\infty$	$Re_\theta$	$Re_\tau$	$T_w/T_r$	$L_{\text{int}}/\delta_0$	$\Delta x^+$	$\Delta y_w^+$	$\Delta y^+$	$\Delta z^+$	$N_x \times N_y \times N_z$
Quasi-adiabatic	2.28	5129	909	1.0	5.33	4.35	0.44	5.26	4.35	$5501 \times 388 \times 611$
Heated	2.28	5244	412	2.0	8.66	1.86	0.19	2.25	1.86	$5501 \times 388 \times 611$
Cooled	2.28	5066	2149	0.5	3.45	5.34	0.53	6.42	5.34	$11001 \times 643 \times 1211$

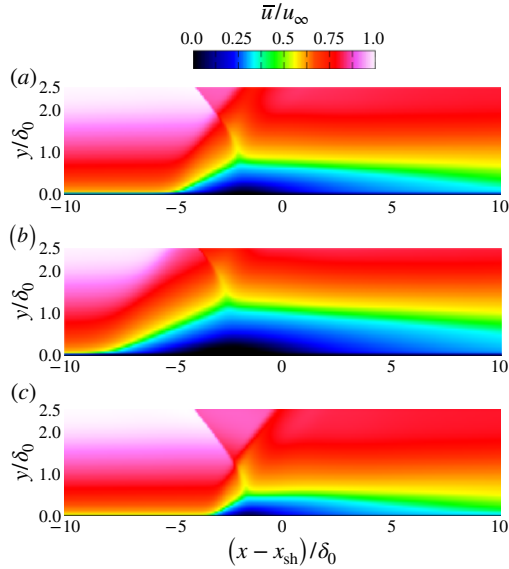


Figure 2. Mean streamwise velocity distributions. (a), Quasi-adiabatic; (b), heated; (c), cooled.

robustly with the compact scheme (Kawai *et al.*, 2010). Also, the third-order TVD Runge-Kutta method is used to conduct time integration explicitly (Gottlieb & Shu, 1998).

The flow and grid parameters of the present cases are summarized in Tab. 1. The Reynolds number and grid resolutions are extracted from  $x = 12\delta_0$  upstream of shock impingement location  $x_{\text{sh}}$ . The interaction length  $L_{\text{int}}$  is obtained as the length between shock impingement location  $x_{\text{sh}}$  and the origin of the reflected shock. Wall heating or cooling decided by  $T_w/T_r$  affect the wall density and viscosity based on Eqs. (4) and (7), which changes friction Reynolds number  $Re_\tau$  significantly between the cases, compared to Reynolds number of boundary-layer momentum thickness  $Re_\theta$ . In the streamwise and spanwise direction, the uniform grids are employed. In the wall-normal direction, the grid spacing is stretched from the wall up to the outer boundaries, where the grid growth rate is approximately 1.03 at the inner boundary layers. The spatial resolutions of the computational grids are comparable to those used in the prior work of DNS (Bernardini *et al.*, 2016).

## RESULTS

### Mean flow fields affected by wall temperature

Figure 2 shows the mean velocity distributions of the present cases. The streamwise location is represented as the non-dimensional distance from shock impingement location  $x_{\text{sh}}$ . Shock-induced separations are observed in all the cases; the separated regions grow in the heated case and shrink in the cooled case, compared with the adiabatic case. Also, the separation points move upstream and downstream in the heated

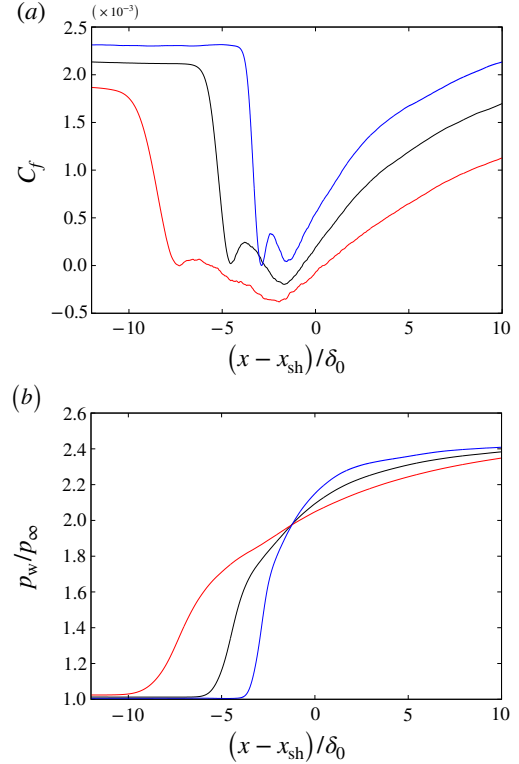


Figure 3. Streamwise distributions of mean (a) skin friction and (b) wall pressure. Black, quasi-adiabatic; red, heated; blue, cooled.

and cooled cases, respectively. The results in Fig. 2 indicate that wall cooling is to the benefit of preventing flow separations, and the differences in the behaviors of shock-induced separated flows appear in the streamwise distributions of wall quantities in Fig. 3. In Fig. 3 (a), the skin friction decreases by flow separations, and the distributions show lower and higher values in the heated and cooled cases, respectively. Also, two peaks are observed for each wall temperature case; the peaks become sharply as wall temperature decreases, and the downstream peaks are located at  $(x - x_{\text{sh}})/\delta_0 \approx -2$  regardless of the wall temperatures. The prior study reported that the existences and sharpness of the upstream peak are dependent on the Reynolds number (Morgan *et al.*, 2013), therefore, the profiles in Fig. 3 (a) are considered to involve the effects of the Reynolds number differences shown in Tab. 1. In Fig. 3 (b), the streamwise gradients of pressure jump at the starting point of boundary layer separations get smaller and larger in the heated and cooled case, respectively. The pressure jump corresponds with a reflected shock that generates low-frequency wall pressure fluctuations, as discussed later in Fig. 7.

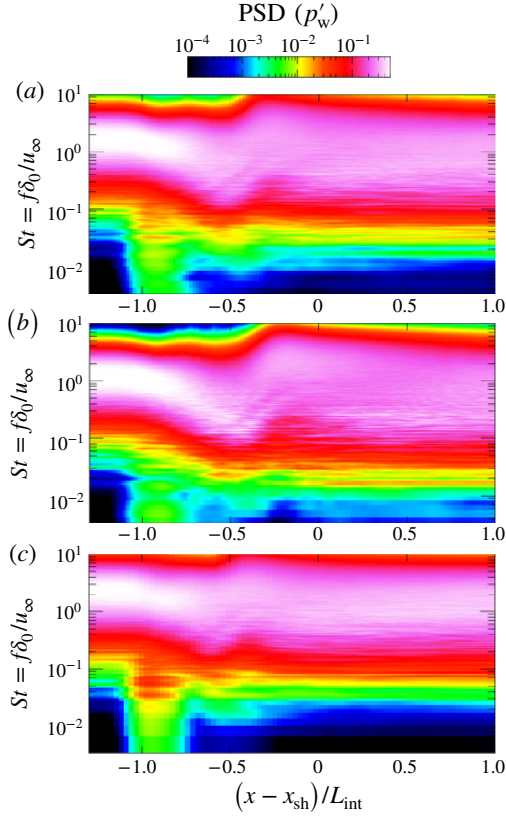


Figure 4. Power spectral density distributions of wall pressure. (a), Quasi-adiabatic; (b), heated; (c), cooled.

### Wall temperature effects on low frequency fluctuations

Figure 4 shows premultiplied power spectral density distributions of the wall pressure as a function of streamwise location and Strouhal number  $St = f\delta_0/u_\infty$ . The streamwise distances from shock impingement location  $x_{sh}$  are scaled by interaction length  $L_{int}$  of each wall temperature case to line up the reflected shock locations. The spectral components are non-dimensionalized by the integral over the entire frequency ranges for each streamwise location. In Fig. 4, the spectral distributions roughly can be divided into two components: low- and high-frequency components. Regarding low-frequency components, spectral density of  $St \sim O(10^{-2})$  is observed at  $(x - x_{sh})/L_{int} \approx -1.0$  in all the cases. In high-frequency regions, dominant spectral distributions at  $St \sim O(10^0)$  are observed throughout the streamwise locations. Also, the overall spectral distributions shift to lower and higher frequencies in the heated and cooled case, respectively.

Next, contributions of the low- and high-frequency components to mean wall pressure fluctuations are evaluated. By performing the inverse Fourier transformation, instantaneous pressure fluctuations are divided into the low- and high-frequency components as,

$$p' = p'_{lf} + p'_{hf}, \quad (9)$$

where the subscripts lf and hf denote quantities consisting of low- and high-frequency components, respectively. The boundary of low- and high-frequency is decided as  $St = f\delta_0/u_\infty = 0.05$ , where  $f$  is the frequency. The pressure fluctuations in Eq. (9) are averaged in time and spanwise direction,

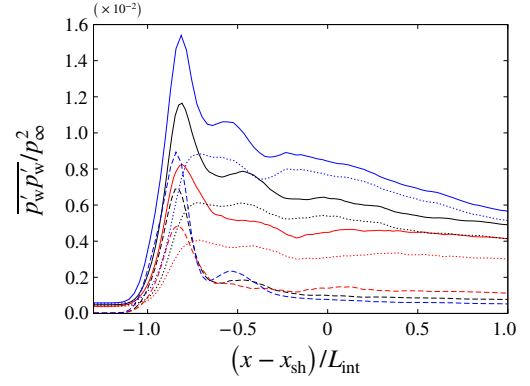


Figure 5. Distributions of wall pressure fluctuations divided into the components in Eq. (10). Solid, LHS; dashed, 1st term of RHS; dotted, 3rd term of RHS. Black, quasi-adiabatic; red, heated; blue, cooled.

and the root-mean-square can be obtained as,

$$\overline{p'p'} = \overline{p'_{lf}p'_{lf}} + 2\overline{p'_{lf}p'_{hf}} + \overline{p'_{hf}p'_{hf}}. \quad (10)$$

Note that the cross-term of low- and high-frequency quantities are small enough to be ignored. Figure 5 shows streamwise distributions of wall pressure fluctuations corresponding to the terms in Eq. (10). The solid lines consisting of all frequency components (LHS in Eq. (10)) show the peak at  $(x - x_{sh})/L_{int} \approx -0.8$  that gets larger as wall temperature decreases. At the same streamwise location, the low-frequency components (1st term of RHS in Eq. (10), dashed lines) also show the peaks, although the high-frequency components (3rd term of RHS in Eq. (10), dotted lines) increase smoothly without the remarkable peak. The results indicate that the maximum peak of wall pressure fluctuations consists of the low-frequency components. Also, comparing the wall temperature cases, a higher peak value of the low-frequency components is observed in the cooled case than in the quasi-adiabatic and heated cases. The results suggest that wall cooling has the disadvantage of providing strong low-frequency wall pressure fluctuations, although the flow separations are prevented compared with quasi-adiabatic and heated wall cases.

Finally, flow phenomena corresponding to the low- and high-frequency wall pressure fluctuations are detected. Instantaneous fields of streamwise velocity and pressure in the quasi-adiabatic case, consisting of the low- or high-frequency fluctuations as Eq. (9), are shown in Fig. 6. Regarding the streamwise velocity distributions (left columns), flow fields, including low-frequency fluctuations, in Fig. 6 (c) show overall structures of boundary layer separations. On the other hand, fine turbulent structures can be seen in the flow fields, including high-frequency fluctuations, in Fig. 6 (e). In the pressure fields (right columns), the fluctuations of separated shear layers are obtained as the high-frequency components in Fig. 6 (f), compared to the low-frequency components in Fig. 6 (d). The results suggest that high-frequency fluctuations of the flow and pressure fields are associated with turbulent structures of the separated shear layers. Also, low-frequency fluctuations seem to contain large-scale motion of overall boundary layer separations.

To discuss the flow physics associated with low- and high-frequency fluctuations more statistically, the frequency components of streamwise velocity and pressure fluctuations are

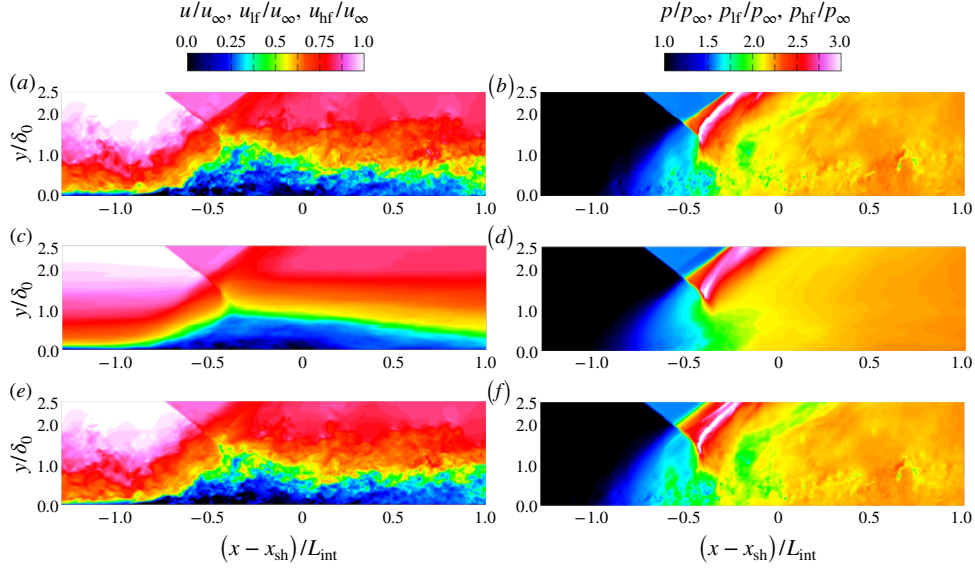


Figure 6. Instantaneous flow fields of streamwise velocity (left columns) and pressure (right columns) in the quasi-adiabatic case, consisting of low- and high-frequency fluctuations as Eq. (9). (a,b), original instantaneous flow fields; (c,d), flow fields consisting of low-frequency fluctuations; (e,f), flow fields consisting of high-frequency fluctuations.

extracted as,

$$\overline{(q'q')}_{lf} = \int_{f_{\min}}^{f_{\text{cri}}} P(f)df, \quad (11)$$

$$\overline{(q'q')}_{hf} = \int_{f_{\text{cri}}}^{f_{\max}} P(f)df, \quad (12)$$

where  $q$  is the flow quantities of streamwise velocity or pressure and  $P$  is the power spectral density of corresponded flow quantities. The subscripts min and max denote the minimum and maximum frequency of used time-stepping data, respectively. Criterion frequency  $f_{\text{cri}}$  is set to  $St = f_{\text{cri}}\delta_0/u_\infty = 0.05$  that is the same boundary used in Eq. (9). Figure 7 shows distributions of streamwise velocity (left columns) and pressure (right columns) fluctuations, extracted by Eqs. (11) and (12), in the quasi-adiabatic case. In Fig. 7 (a) of low-frequency streamwise velocity fluctuations, overall flow separations are highlighted. Also, in Fig. 7 (b) of low-frequency pressure fluctuations, impinging and reflected shock are observed. Especially in the reflected shock, the distributions extend to the lower wall at streamwise location  $(x - x_{\text{sh}})/L_{\text{int}} \approx -1.0$ , suggesting that low-frequency components of wall pressure fluctuations shown in Figs. 4 and 5 are associated with the reflected shock motion. As shown in Fig. 3 (b), the pressure gradients of reflected shock change between the wall temperature cases, which can be considered to affect the differences in low-frequency wall pressure fluctuations in Fig. 5. On the other hand, the high-frequency fluctuations in Figs. 7 (c) and (d) distribute at separated shear layers, which are consistent with the observation in Fig. 6. Also, near-wall turbulence at attached boundary layer regions is highlighted in Figs. 7 (c). The results suggest that turbulent structures at attached boundary layers and separated shear layers provide the spectral components at  $St \sim O(10^0)$  in Fig. 4. Regarding near-wall turbulence at attached turbulent boundary layers, a previous study shows that the length scales of turbulent structures in thermal turbulent boundary layers depend on the differences in the semi-local Reynolds number, regardless of the temperature, density, and viscosity themselves (Hirai *et al.*, 2021). Furthermore,

turbulent structures in separated shear layers also can be affected by the semi-local Reynolds number because separated shear layers originate from the separation of incoming turbulent boundary layers. Thus, the changes of friction Reynolds number by wall heating and cooling, shown in Tab. 1, can be one of the causes of the high-frequency spectral distribution shifts observed in Fig. 4.

## CONCLUSIONS

In this study, wall heating and cooling effects on low-frequency dynamics in the shock-wave and turbulent boundary layer interactions were investigated by direct numerical simulations. Power spectral density of the wall pressure showed that the low-frequency fluctuations happen locally at the starting point of boundary layer separations, although the high-frequency components distribute throughout the streamwise locations. By dividing the root-mean-square of wall pressure into the low- and high-frequency components, large contributions of the low-frequency components to the maximum peak of wall pressure fluctuations were elucidated. The peak of the low-frequency wall pressure fluctuations gets larger in the cooled wall cases, suggesting that wall cooling has some undesirable contributions to decreasing the low-frequency wall pressure fluctuations that can lead to structural fatigue. Furthermore, to detect flow physics associated with the low- and high-frequency wall pressure fluctuations, the corresponding frequency fluctuations of streamwise velocity and pressure fields were observed. Distributions of the low-frequency streamwise velocity and pressure fluctuations indicate that overall boundary layer separations and reflected shock are associated with the low-frequency wall pressure fluctuations. Regarding the reflected shock, differences in pressure gradients are observed between the wall temperature cases, which can change low-frequency wall pressure fluctuations. Also, high-frequency fluctuations of streamwise velocity and pressure distribute at separated shear layers and near-wall regions of attached boundary layers. The semi-local Reynolds number effects on near-wall turbulence, reported in a previous study, are considered to affect the frequency shifts of wall

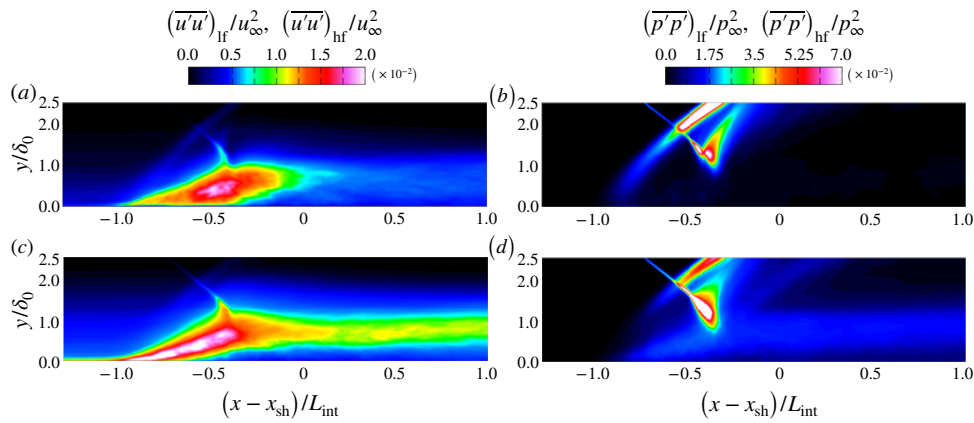


Figure 7. Distributions of streamwise velocity (left columns) and pressure (right columns) fluctuations in the quasi-adiabatic case, obtained by Eqs. (11) and (12). (a,b), low-frequency components of Eq. (11); (c,d), high-frequency components of Eq. (12).

pressure spectral distributions at high-frequency regions. In future work, we will investigate clear contributions of pressure gradients of reflected shock and semi-local Reynolds number, which are changed by wall heating and cooling, to low- and high-frequency wall pressure fluctuations, respectively.

## ACKNOWLEDGEMENTS

This work was supported in part by Japan Society for the Promotion of Science Grant-in-Aid for Scientific Research (B) KAKENHI 21H01523. A part of this research used computational resources of the Fugaku computer provided by the RIKEN Advanced Institute for Computational Science. (Project ID: hp210099 and hp220034).

## REFERENCES

- Bernardini, M., Asproulias, I., Larsson, J., Pirozzoli, S. & Grasso, F. 2016 Heat transfer and wall temperature effects in shock wave turbulent boundary layer interactions. *Physical Review Fluids* **1**, 084403.
- Brusniak, L. & Dolling, D. S. 2006 Physics of unsteady blunt-fin-induced shock wave/turbulent boundary layer interactions. *Journal of Fluid Mechanics* **273**, 375–409.
- Clemens, N. T. & Narayanaswamy, V. 2014 Low-frequency unsteadiness of shock wave/turbulent boundary layer interactions. *Annual Review of Fluid Mechanics* **46**, 469–492.
- Deck, Sébastien 2009 Delayed detached eddy simulation of the end-effect regime and side-loads in an overexpanded nozzle flow. *Shock Waves* **19**, 239–249.
- Gaitonde, D. & Visbal, M. 1999 Further development of a navier-stokes solution procedure based on higher-order formulas. In *37th Aerospace Sciences Meeting and Exhibit*, pp. 99–0557. Reno, NV: American Institute of Aeronautics & Astronautics.
- Ganapathisubrama, B., Clemens, N. T. & Dolling, D. S. 2007 Effects of upstream boundary layer on the unsteadiness of shock-induced separation. *Journal of Fluid Mechanics* **585**, 369–394.
- Ganapathisubrama, B., Clemens, N. T. & Dolling, D. S. 2009 Low-frequency dynamics of shock-induced separation in a compression ramp interaction. *Journal of Fluid Mechanics* **636**, 397–425.
- Gottlieb, S. & Shu, C. W. 1998 Total variation diminishing runge-kutta schemes. *Mathematics of Computation* **67**, 73–85.
- Hirai, R., Pecnik, R. & Kawai, S. 2021 Effects of the semi-local reynolds number in scaling turbulent statistics for wall heated/cooled supersonic turbulent boundary layers. *Physical Review Fluids* **6**, 124603.
- Jaunet, V., Debiève, J. F. & Dupont, P. 2014 Length scales and time scales of a heated shock-wave/boundary-layer interaction. *AIAA Journal* **52**, 2524–2532.
- Kawai, S. & Fujii, K. 2008 Compact scheme with filtering for large-eddy simulation of transitional boundary layer. *AIAA Journal* **46** (3), 690–700.
- Kawai, S., Shankar, S. K. & Lele, S. K. 2010 Assessment of localized artificial diffusivity scheme for large-eddy simulation of compressible turbulent flows. *Journal of Computational Physics* **229**, 1739–1762.
- Lele, S. K. 1992 Compact finite difference schemes with spectral-like resolution. *Journal of Computational Physics* **103**, 16–42.
- Morgan, B., Duraisamy, K., Nguyen, N., Kawai, S. & Lele, S. K. 2013 Flow physics and rans modelling of oblique shock/turbulent boundary layer interaction. *Journal of Fluid Mechanics* **729**, 231–284.
- Piponnier, S., Dussauge, J. P., Debiève, J. F. & Dupont, P. 2009 A simple model for low-frequency unsteadiness in shock-induced separation. *Journal of Fluid Mechanics* **629**, 87–108.
- Pirozzoli, S. & Grasso, F. 2006 Direct numerical simulation of impinging shock wave/turbulent boundary layer interaction at  $m=2.25$ . *Physics of Fluids* **18**, 065113.
- Simens, M. P., Jimnez, J., Hoyas, S. & Mizuno, Y. 2009 A high-resolution code for turbulent boundary layers. *Journal of Computational Physics* **228**, 4218–4231.
- Touber, E. & Sandham, N. D. 2011 Low-order stochastic modelling of low-frequency motions in reflected shock-wave/boundary-layer interactions. *Journal of Fluid Mechanics* **671**, 417–465.
- Urbain, G. & Knight, D. 2001 Large-eddy simulation of a supersonic boundary layer using an unstructured grid. *AIAA Journal* **39**, 1288–1295.
- Volpiani, P. S., Bernardini, M. & Larsson, J. 2018 Effects of a nonadiabatic wall on supersonic shock/boundary-layer interactions. *Physical Review Fluids* **3**, 083401.